NANO LETTERS
Letter
Cite This: Nano Lett. 2019, 19, 3011−3018
pubs.acs.org/NanoLett

# Direct Synthesis of Water-Dispersible Magnetic/Plasmonic Heteronanostructures for Multimodality Biomedical Imaging

Jingbin Zeng,[*,†,‡] Mingfu Gong,[‡,§] Dawei Wang,[‡] Mengmeng Li,[†] Wenjing Xu,[‡] Zhiwei Li,[‡] Shichuan Li,[‡] Dong Zhang,[*,§] Zifeng Yan,[†] and Yadong Yin[*,‡]

[†]College of Science, China University of Petroleum (East China), Qingdao 266580, China
[‡]Department of Chemistry, University of California, Riverside, California 92521, United States
[§]Department of Radiology, Xinqiao Hospital, Army Medical University, Chongqing 400037, China

Supporting Information

**ABSTRACT:** Magnetic/plasmonic hybrid nanoparticles are highly desirable for multimodal bioimaging and biosensing. Although the synthesis of heterodimeric nanoparticles has been reported, the products are usually hydrophobic so that post-treatment procedures are required to transfer them into water which are often difficult to perform and cause damages to the structures. Direct synthesis of hydrophilic hybrid nanostructures has remained a grand challenge albeit its immediate advantage of biocompatibility. Herein we report a general seed-mediated approach to the synthesis of hydrophilic and biocompatible M−$Fe_3O_4$ (M = Au, Ag, and Pd) heterodimers, in which the size of metals and $Fe_3O_4$ can be independently regulated in a wide range. Benefiting from the aqueous synthesis, this approach can be further extended to design more complex heterodimeric structures such as $AgPt_{alloy}$−$Fe_3O_4$, $Au_{core}$@$Pd_{shell}$−$Fe_3O_4$, and $Au_{shell}$−$Fe_3O_4$. The hydrophilic nature of our heterodimers makes them readily useful for biomedical applications without the need of additional ligand exchange processes in contrast to those prepared in nonpolar solvents. These nanoscale magnetic/plasmonic heterostructures were shown to be ideally suited for integrated biomedical diagnoses, such as magnetic resonance imaging, photoacoustic imaging, optical coherence tomography, and computed tomography, in virtue of their biocompatibility and combined tunable magnetic and plasmonic properties.

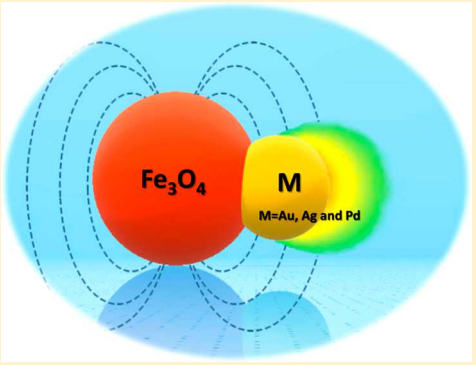


**KEYWORDS:** *Magnetic, plasmonic, heterodimers, magnetic resonance imaging, computed tomography, optical coherence tomography, photoacoustic imaging, multimodality imaging*

Hybrid nanostructures have received considerable attention as they may offer integrated multifunctionalities that are difficult to achieve by a simple mixture of the individual components. A class of hybrid nanostructures that are highly desirable include heterodimers composed of iron oxide and noble metal (Au, Ag, Pd, Pt). With combined magnetic, plasmonic, and catalytic properties, they promise broad potential applications in catalysis,[1−3] optical sensing,[4−6] bioimaging,[7] drug delivery,[8] and electrochemistry.[9] Many groups have explored chemical routes to the successful synthesis of superparamagnetic iron oxide-noble metal heterodimers,[6,8,10−17] however the products are usually capped with a layer of hydrophobic ligands such as oleic acid or oleylamine so that they are not readily soluble in water,[18,19] greatly limiting their biomedical applications. A ligand exchange process is therefore indispensable to bring these nanoparticles (NPs) into water[20] which unfortunately does not always proceed completely so aggregation may frequently occur during further bioconjugation processes. On the other hand, an extensive ligand exchange process may often lead to the breakage of the dimer structures, significantly reducing their functionalities for the intended biomedical applications.

Herein we propose a general seed-mediated approach to the synthesis of M−$Fe_3O_4$ (M = Au, Ag and Pd) heterodimers directly in an aqueous medium. In this approach, we take advantage of the reductive nature of $Fe_3O_4$ to initiate the reduction of metal cations and deposition of a metal seed on the surface of each $Fe_3O_4$ NP and then grow the metal seed to the desired size through a seed-mediated process. By separating the formation of the two components, we could control the sizes of the $Fe_3O_4$ and metal NPs independently, producing heterodimers with highly configurable compositions and structures. Benefiting from the aqueous synthesis, the resulting heterodimers are soluble in water and show excellent biocompatibility, making them ideal dual-mode contrast agents for magnetic resonance imaging (MRI) and computed tomography (CT) imaging. In addition, the metal NPs can

**Received:** January 14, 2019
**Revised:** March 24, 2019
**Published:** April 11, 2019






DOI: 10.1021/acs.nanolett.9b00171
Nano Lett. 2019, 19, 3011−3018

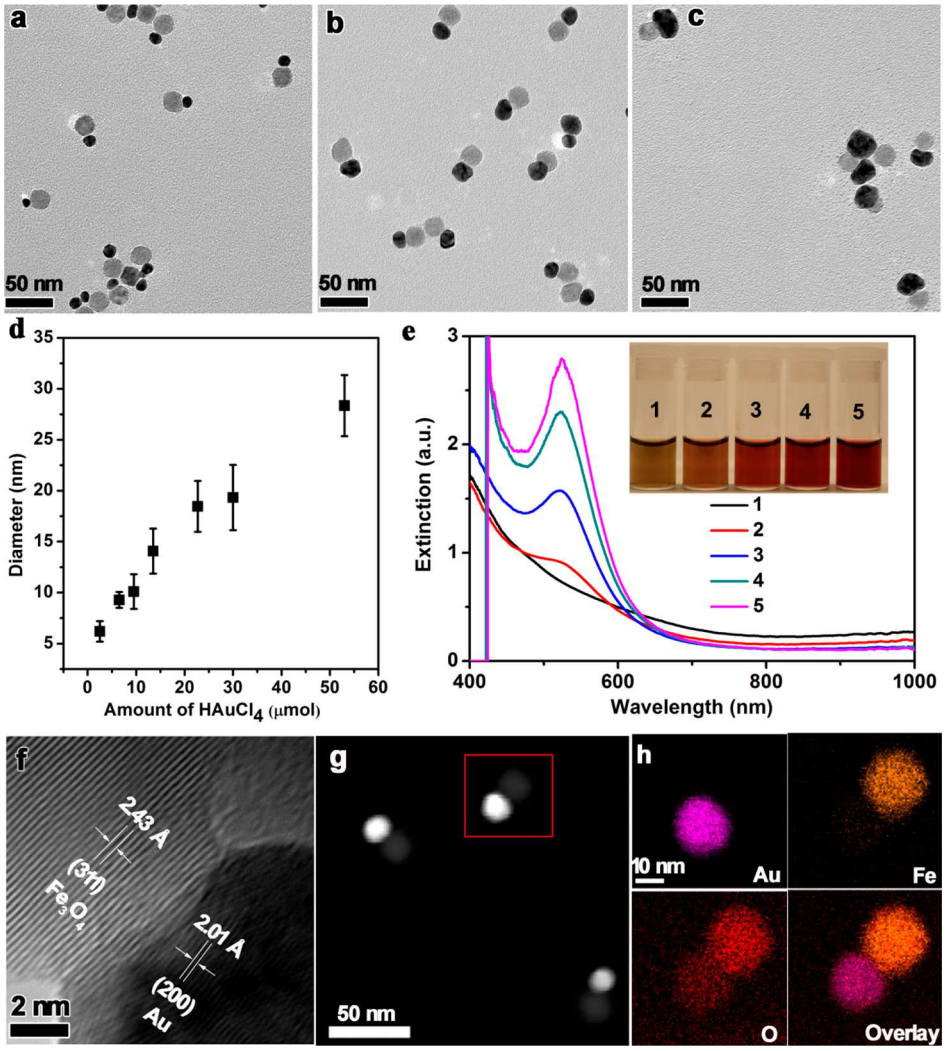


**Figure 1.** (a–c) TEM of Au–$Fe_3O_4$ heterodimers with different gold size. (d) Size distribution of Au in the heterodimers in relation to the amount of $HAuCl_4$. (e) The UV–vis spectra and corresponding photo (inset) of $Fe_3O_4$ NPs (1) and Au–$Fe_3O_4$ heterodimers (2–5, the size of Au increases from samples of 2 to 5). (f) HRTEM, (g) HAADF-STEM, and (h) STEM elemental maps of Au, Fe, O, and their overlay.

be further engineered through seeded growth or galvanic replacement to produce more complex heterodimer structures such as $AgPt_{alloy}$–$Fe_3O_4$, $Au_{core}@Pd_{shell}$–$Fe_3O_4$, and $Au_{shell}$–$Fe_3O_4$, that not only enable their use as excellent contrast agents in more imaging modalities, such as optical coherence tomography (OCT) and photoacoustic (PA) but are also expected to expand their application to areas such as catalysis and sensing.

The success of this approach was first demonstrated by the synthesis of Au–$Fe_3O_4$ heterodimers. Water-soluble $Fe_3O_4$ NPs were synthesized through a pyrolysis reaction using oleic acid as the capping ligand in a $N_2$ atmosphere, followed by surface treatment using tetramethylammoniumhydroxide (TMAH) in air which made the NPs soluble in water.[21] The as-synthesized $Fe_3O_4$ NPs were single crystalline and monodispersed, as seen in Figure S1 of a typical sample (19.8 ± 1.3 nm). X-ray photoelectron spectroscopy (XPS) analysis (Figure S2) reveals that there are two peaks centering at 723.4 and 709.8 eV, which can be designated to Fe 2p1/2 and Fe 2p3/2 of $Fe_3O_4$, respectively.[22,23] The broadening of Fe 2p peaks is caused by the presence of dual iron oxidation states of $Fe^{3+}$ and $Fe^{2+}$, which exhibit an atomic ratio of 63.6%:36.4% based on the XPS result shown in Figure S2. Upon adding a gold precursor ($HAuCl_4$) to a boiling aqueous solution of $Fe_3O_4$ NPs and sodium citrate, the $Fe^{2+}$ on the surface of $Fe_3O_4$ reduced the Au(III) to Au(0) and thus led to the deposition of a small Au seed on each $Fe_3O_4$ NP. Figure S3 shows a typical sample of the resulting Au–$Fe_3O_4$ heterodimers with the average size of Au seeds of 4.5 nm and a dimer yield of 80.5% as estimated by counting 435 particles. Additional Au precursor and reducing agent can be added to the system to initiate further growth of AuNPs to the desired sizes. Figure 1a–c shows a few examples of heterodimers with AuNP size varying from 9.5 to 28.2 nm, and the dependence of Au size on the amounts of $HAuCl_4$ is summarized in Figure 1d. On the other hand, the size of the $Fe_3O_4$ NPs can be adjusted separately during their original synthesis, as demonstrated in Figure S4 by the two additional samples with $Fe_3O_4$ NPs of 14 and 38 nm. The Au–$Fe_3O_4$ heterodimers exhibited a plamonic peak at 520 nm, which gradually enhanced with the size of the AuNPs (Figure 1e). The high-resolution transmission electron microscopy (HRTEM) image in Figure 1f shows that both $Fe_3O_4$ and Au were single crystals and the interface between them appears to be coherent. The lattice spacings in the light and dark sections were measured to be 2.43 and 2.01 Å, corresponding to the (311) planes of the cubic magnetite and



DOI: 10.1021/acs.nanolett.9b00171
*Nano Lett.* 2019, 19, 3011–3018

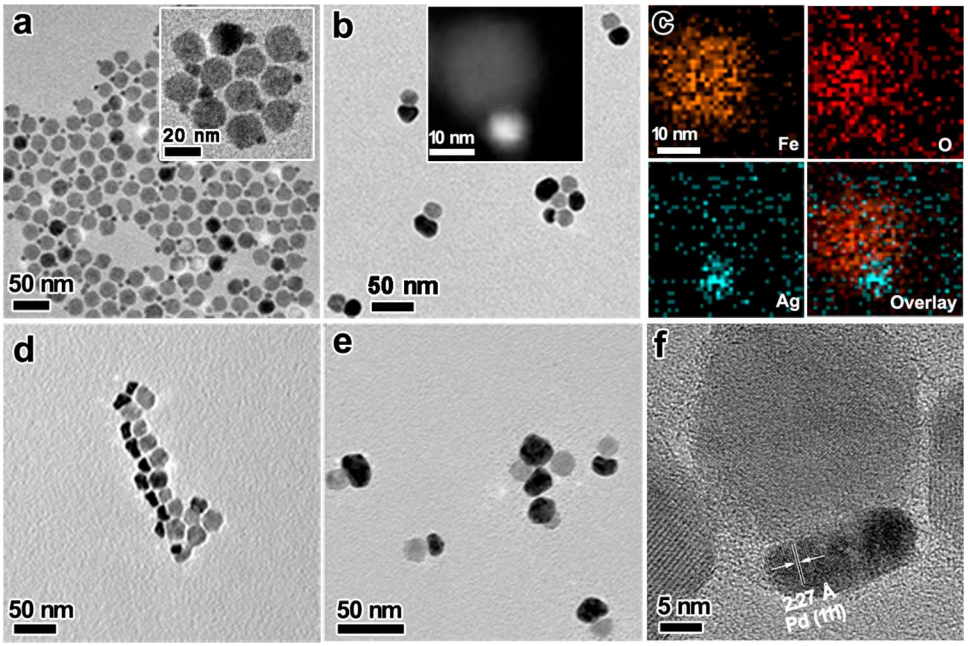


**Figure 2.** (a,b) TEM images of Ag−$Fe_3O_4$ heterodimers with varying Ag sizes. (c) STEM elemental mapping of the sample in (a). (d,e) TEM images of Pd−$Fe_3O_4$ heterodimers with varying Pd sizes. (f) HRTEM of the sample in (d). The inset in (a) shows the particles at a higher magnification, and the inset in (b) shows a HAADF-STEM image of a typical Ag−$Fe_3O_4$ heterodimer.

(200) planes of the face-centered cubic (fcc) Au, respectively. The crystal structure of the heterodimers was further verified by the XRD patterns shown in Figure S5. The heterodimer structure was further verified by the high-angle annular dark-field scanning transmission electron microscopy (HAADF-STEM) which revealed a reverse contrast to the HRTEM image as expected (Figure 1g) and by elemental mapping based on the HAADF-STEM-energy-dispersive X-ray spectroscopy (EDS) which confirmed the presence of Au, Fe, and O elements in each heterodimer (Figure 1h).

To investigate the formation mechanism of the heterodimers, we collected aliquots at the reaction time of 5 s, 2 min, 5 min, and 30 min for TEM analysis. As shown in Figure S6, the heterodimer structures were formed at the very early stage of the reaction. However, some very small AuNPs (1.2 ± 0.3 nm) could also be observed at 5 s, which quickly disappeared after 2 min of reaction due to Ostwald ripening. As indicated in Figure S7, the characteristic plasmonic peak of AuNPs gradually enhanced as the reaction proceeded. In contrast, simply mixing the $Fe_3O_4$ NPs with $HAuCl_4$ in the absence of trisodium citrate (TSC) led to the deposition of a number of small AuNPs onto the surface of $Fe_3O_4$ NPs and formed a satellite structure rather than a dimer (Figure S8). Adding TSC afterward did not produce dimers but very large AuNPs upon extended heating. On the basis of the above observations, we can infer the following formation mechanism. At the initial stage of the reaction, Au(III) is reduced quickly by near-surface $Fe^{2+}$ to yield one or possibly more Au seeds on the surface of each $Fe_3O_4$ particle. When the surface $Fe^{2+}$ is consumed, a slower reduction by TSC continues to generate Au(0) to support the further growth of the AuNPs. A ripening process will preferentially dissolve the smaller seeds deposited on the $Fe_3O_4$ particles and also those free ones produced by TSC reduction, thereby promoting the growth of one relatively larger AuNP attached to each $Fe_3O_4$ NP.

The reductivity of $Fe_3O_4$ was further confirmed by the fact that AuNPs can be generated similarly on the surface of multicrystalline $Fe_3O_4$ nanocrystal clusters and hollow nanorods that we reported previously (Figure S9),[24] although the products were not well-defined dimers due to the insufficient ripening of Au on large $Fe_3O_4$ particles. In contrast, when $\beta$-FeOOH nanorods, which were the precursors to the $Fe_3O_4$ nanorods,[24] were used, only large free AuNPs could be observed. These results clearly indicate that the presence of $Fe^{2+}$ is a key factor to initiate the preferential deposition of Au on the surface of $Fe_3O_4$ to form heterodimers. On the other hand, when the surface ligand on $Fe_3O_4$ was changed from TMAH to poly(acrylic acid), Au−$Fe_3O_4$ heterodimers could still be obtained (Figure S10), indicating that the surface ligands played a nonessential role in the formation of the dimer structure.[3]

To demonstrate the generality of this approach, we extended it to the preparation of Ag−$Fe_3O_4$, Pd−$Fe_3O_4$, and Pt−$Fe_3O_4$ heterostructures. For the Ag−$Fe_3O_4$ system, it was found that many small AgNPs were present around the surface of $Fe_3O_4$ NPs (Figure S11), suggesting insufficient Ostwald ripening. For promoting the ripening, UV irradiation at 258 nm was applied, which successfully converted the products into monodispersed Ag−$Fe_3O_4$ heterodimers with a yield of 88.9% based on the counting of 205 particles (Figure 2a, Figure S11). The dimer structure was confirmed again by elemental mapping (Figure 2c) and XRD (Figure S12). Similarly, Pd−$Fe_3O_4$ heterodimers could be synthesized, as confirmed by HRTEM and XRD analyses (Figure 2f, Figure S12). Again, the seed-mediated growth strategy allowed variation of the size of the metal parts, as demonstrated in Figure 2a,b, and Figure 2d,e where the size of Ag and Pd were tuned from 3.8 to 20.5 nm and 6.2 to 15.4 nm, respectively. The same approach could be applied to deposit PtNPs onto the surface of $Fe_3O_4$ NPs to produce heterostructures (Figure S13). However, due to the high chemical stability of Pt,



DOI: 10.1021/acs.nanolett.9b00171
*Nano Lett.* 2019, 19, 3011−3018

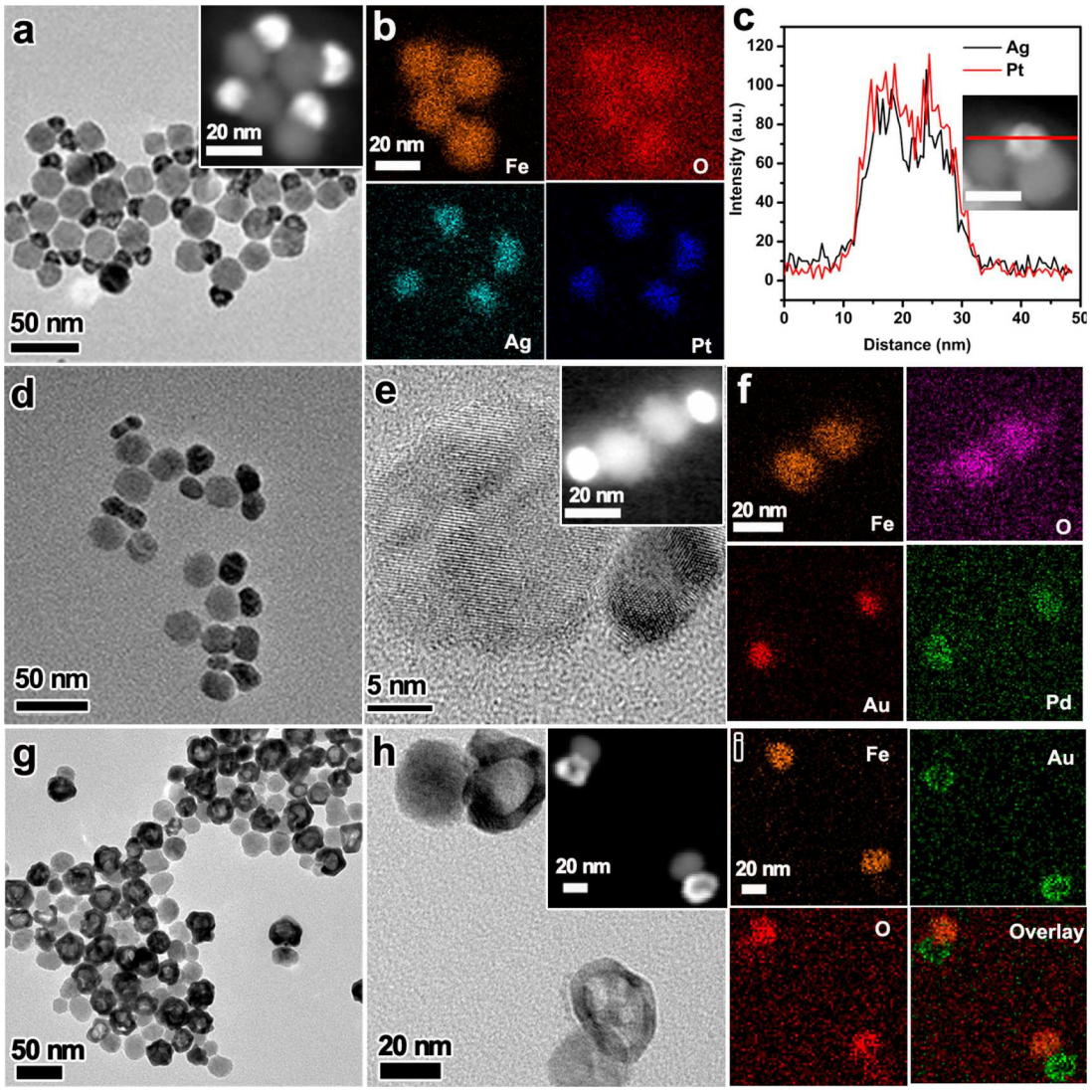


**Figure 3.** (a) TEM and STEM-HAADF (inset) images of $AgPt_{alloy}$–$Fe_3O_4$ heterodimers. (b) STEM elemental maps of Fe, O, Ag, and Pt of the sample in the inset in (a). (c) Cross-sectional compositional line profile of an $AgPt_{alloy}$–$Fe_3O_4$ heterodimer obtained from the red line in the inset in (c). (d,e) TEM (d), HRTEM (e), and STEM-HAADF (inset in (e)) images of $Au_{core}$@$Pd_{shell}$–$Fe_3O_4$ heterodimers. (f) STEM elemental maps of Fe, O, Au, and Pd of the sample in the inset in (e). (g,h) TEM and STEM-HAADF (inset in h) images of $Au_{shell}$–$Fe_3O_4$ heterodimers. (i) STEM elemental maps of Fe, O, Au and their overlay of the heterodimers shown in the inset in (h).

Ostwald ripening did not occur efficiently under the reaction condition so that the PtNPs remained as small satellites around the $Fe_3O_4$ NPs.

Compared with the synthesis in nonpolar phases, our process takes place in aqueous solution so that additional redox reactions can be easily initiated on the heterodimers to generate more complex architectures. We first demonstrated the use of Ag–$Fe_3O_4$ heterodimers as the precursor to synthesize $AgPt_{alloy}$–$Fe_3O_4$ heterodimers through the galvanic replacement reaction between Ag and $[PtCl_4]^{2-}$.[25] Figure 3a confirms the dimeric structure, while the elemental mapping results in Figure 3b,c verify the alloy nature of the AgPt part. We further demonstrated the deposition of Pd on to the surface of Au in Au–$Fe_3O_4$ heterodimers and yielded $Au_{core}$@$Pd_{shell}$–$Fe_3O_4$ heterodimers. The TEM and HRTEM images (Figure 3d,e) show that the dark areas in the new heterostructures are larger than those in the original Au–$Fe_3O_4$ heterodimers (Figure 1a), suggesting the coating of Pd onto the Au surface which is further confirmed by elemental mapping (Figure 3f, Figure S14). The last example was the construction of $Au_{shell}$–$Fe_3O_4$ heterodimers by first depositing a layer of Au to the surface of Ag in the Ag–$Fe_3O_4$ heterodimers through the galvanic reaction, then etching away Ag by $H_2O_2$.[26−28] As shown in Figure 3g,h, the as-synthesized heterodimer consists of a solid sphere attached by a hollow shell, which were confirmed as $Fe_3O_4$ and Au, respectively, based on the EDS mapping results (Figure 3i).

The hydrophilic nature of our heterodimers makes them readily useful for biomedical applications without the need of additional ligand exchange processes, which is in contrast to those prepared in nonpolar solvents. For verification purpose, the potential cytotoxicity of Au–$Fe_3O_4$ heterodimers was examined by coculture with human nonsmall cell lung cancer cells A549. The heterodimers showed ignorable toxicity to the A549 cells in the CCK-8 analysis. Even after coincubation with the heterodimers (0.5 mg/mL) for 48 h, the cells remained similar viability to the control group (Figure S15a). To further quantitatively study the cellular toxicity, we counted the



DOI: 10.1021/acs.nanolett.9b00171
*Nano Lett.* 2019, 19, 3011−3018

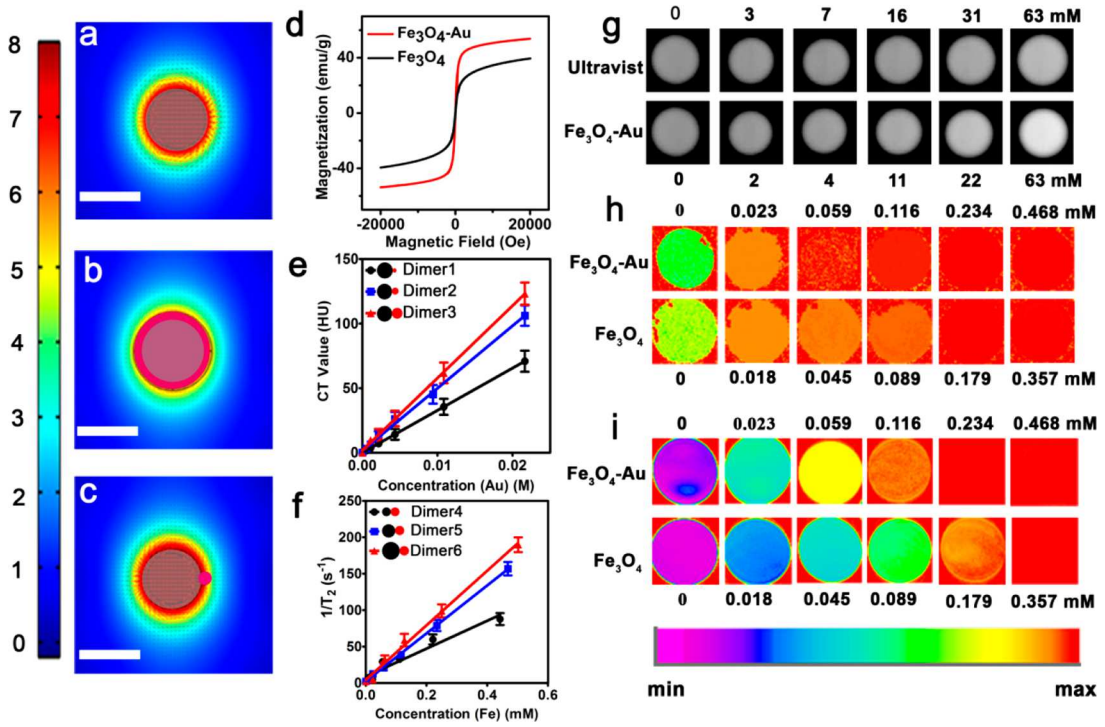


**Figure 4.** Distribution of simulated magnetic field induced by (a) $Fe_3O_4$ (b) core−shell $Fe_3O_4$@Au NPs and (c) Au−$Fe_3O_4$ heterodimers. (The scale bar is 20 nm.) (d) The hysteresis loop of $Fe_3O_4$ NPs and Au−$Fe_3O_4$ heterodimers. (e) The linear fitting of CT value and various concentrations of Au−$Fe_3O_4$ heterodimers with different size of Au. (The sizes of Au−$Fe_3O_4$ dimers 1, 2, and 3 are 3.6 and 19.8 nm, 7.2 and 19.8 nm, and 11.3 and 19.8 nm, respectively.) (f) The linear fitting of $1/T_2$ and various concentrations of Au−$Fe_3O_4$ heterodimers with different sizes of $Fe_3O_4$. (The sizes of Au−$Fe_3O_4$ in dimers 4, 5, and 6 are 5.0 and 14.5 nm, 4.5 and 19.8 nm, and 12.2 and 38.0 nm, respectively.) (g) The CT images of Ultravist and Au−$Fe_3O_4$ heterodimers with various concentrations. (The concentrations of Au−$Fe_3O_4$ heterodimers in this CT test are given based on the Au element.) (h) The MR $T_2$-weighted and $T_2$-mapping (i) images of $Fe_3O_4$ NPs and Au−$Fe_3O_4$ heterodimers with various concentrations and the color bar. (The concentrations of $Fe_3O_4$ NPs and Au−$Fe_3O_4$ heterodimers in this MRI test are given based the Fe element.)

apoptotic and necrotic A549 cells by flow cytometry following incubation with the heterodimers. Similarly, there was negligible apoptosis and death detected, indicating their good biocompatibility (Figure S15b).

Integrated multimodal imaging techniques can overcome the inherent weaknesses of individual imaging technology and provide complementary information to improve the diagnosis of diseases. For instance, MRI/CT dual-modality imaging has shown immense potential in disease diagnosis because it combines the superb soft tissue resolution of MRI and excellent density resolution of CT.[29−32] $Fe_3O_4$−Au hybrid nanocomposites are considered to be perfect contrast agents for MRI/CT dual-modality imaging because the superparamagnetic $Fe_3O_4$ NPs can significantly shorten the transverse relaxation time ($T_2$) and the AuNPs can notably attenuate X-ray due to its high electron density.[33−36] However, for previously explored $Fe_3O_4$@Au core−shell NPs,[37−39] optimizing both the sensitivity of MRI and CT by tuning the size of the $Fe_3O_4$ core and Au shell could cause the reverse effect. For example, increasing the Au shell thickness might improve the attenuation efficiency but will also lead to a decrease of transverse relaxivity ($r_2$) due to the shielding effect caused by the Au shell (Figure 4a,b).[36] On the contrary, the Au−$Fe_3O_4$ heterodimers can avoid the contradiction and allow optimization of both the sensitivity of MRI and CT as the Au attachment does not significantly separate the protons from the surface of the $Fe_3O_4$ moiety (Figure 4c). More interestingly, as shown in Figure 4d, heterodimers displayed a higher saturation magnetization ($M_s$) of 53.8 emu/g Fe than that of $Fe_3O_4$ NPs (39.5 emu/g Fe). The improved $M_s$ of heterodimers may result from the oxidation of $Fe^{2+}$ by $HAuCl_4$ when the Au seeded on the surface of the $Fe_3O_4$ NPs, converting the residual antiferromagnetic FeO into superparamagnetic $Fe_3O_4$.[40] Accordingly, at the same Fe concentration, the Au−$Fe_3O_4$ heterodimers induced more signal intensity drop and $T_2$ shortening (Figure 4h,i) and showed higher $r_2$ of 370.1 $mM^{-1}$ $s^{-1}$ than that of $Fe_3O_4$ NPs (316.4 $mM^{-1}$ $s^{-1}$) (Figure S16a), indicating its feasibility as an MRI contrast agent. To further evaluate its superiority as a CT contrast agent, a clinically approved iodinated-contrast agent (Ultravist) was selected for comparison. Figure S16b and Figure 4g reveal that the Au−$Fe_3O_4$ heterodimers showed 1.23-fold greater X-ray attenuation efficiency than the Ultravist. Compared with those synthesized in organic solvents where size tuning was often challenging,[41] our approach allows convenient tuning of the sizes of Au and $Fe_3O_4$ NPs separately over a relatively broad range to optimize the MRI and CT imaging sensitivity. As shown in Figure 4e, the heterodimers with larger Au showed a better X-ray attenuation efficiency than those with small ones due to their relatively higher electronic density.[42] Similarly, the heterodimers with the increasing size of $Fe_3O_4$ moiety showed higher transverse relaxivity because of the larger $M_s$ value (Figure 4f).[36]

Under the permission of the Animal Welfare and Ethics Committee of the Army Medical University, the $r_2$ and X-ray attenuation efficiency of the Au−$Fe_3O_4$ heterodimers were evaluated in vivo by MRI and CT studies of rats. The result showed that the signal intensity of liver in $T_2$ weighted image



DOI: 10.1021/acs.nanolett.9b00171
Nano Lett. 2019, 19, 3011−3018

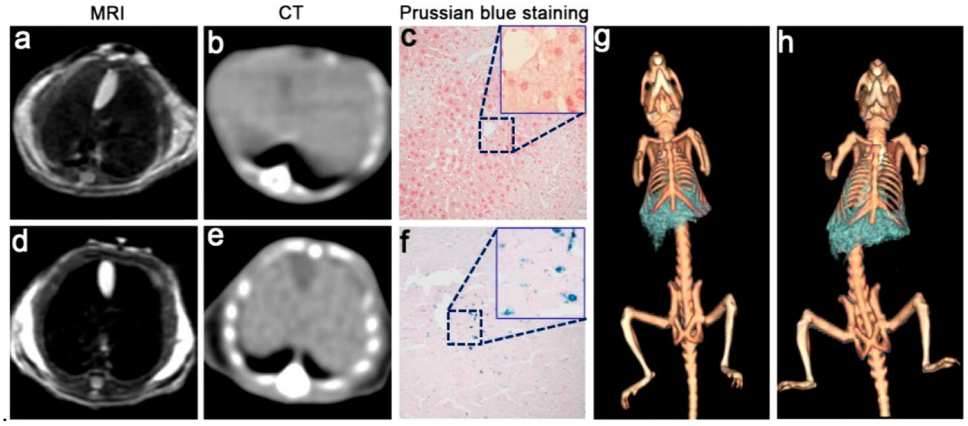


**Figure 5.** (a–f) The MR $T_2$-weighted images, CT images, and the Prussian blue staining images of rat liver before and after the injection of Au–$Fe_3O_4$ (4.5 and 19.8 nm) heterodimer solution: (a) MR image before injection; (b) CT image before injection; (c) Prussian blue staining image (200×) before injection; (d) MR image 30 min after injection; (e) CT image 30 min after injection; (f) Prussian blue staining image (200×) after injection for 30 min. The insets in (c,f) are enlarged images with 400-fold amplification. The volume rendering images of rat liver based on their high-resolution CT images: (g) before and (h) 30 min after the injection of Au–$Fe_3O_4$ heterodimer solution.

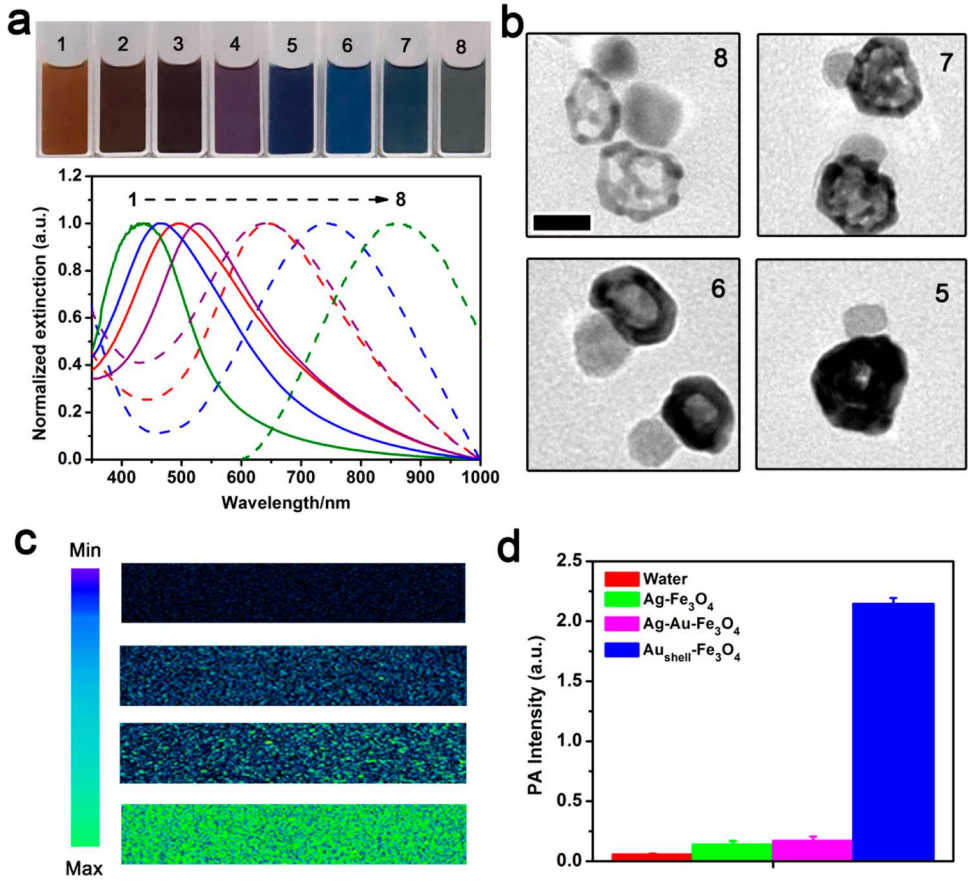


**Figure 6.** (a) Photographs and UV–vis spectra of $Ag_{core}@Au_{shell}$–$Fe_3O_4$ with increasing dimensional ratio of $Au_{shell}$-to-$Ag_{core}$ (sample 1–4) and corresponding $Au_{shell}$–$Fe_3O_4$ heterodimers with increasing dimensional ratio of cavity-to-$Au_{shell}$ (sample 5–8). (b) TEM images of the corresponding $Au_{shell}$–$Fe_3O_4$ heterodimers with increasing dimensional ratio of $Au_{shell}$-to-cavity from 8 to 5 as shown in Figure 1a; the scale bar is 20 nm. (c) OCT B-scan images of pure water and aqueous dispersions of Ag–$Fe_3O_4$, $Ag_{core}@Au_{shell}$–$Fe_3O_4$, and $Au_{shell}$–$Fe_3O_4$ heterodimers with the same particle concentration (from top to bottom). (d) PA intensities of aqueous dispersions containing Ag–$Fe_3O_4$, $Ag_{core}@Au_{shell}$–$Fe_3O_4$, and $Au_{shell}$–$Fe_3O_4$ heterodimers with the same concentration.

was significantly reduced after administration of the heterodimers and the relative MRI signal intensity decreased from 72.3% to 18.9% (Figure 5a,d). In the CT images, the relative CT value increased from 92.4% to 102.3% (Figure 5b,e,g,h). The Prussian blue stain of the rat liver showed that there were many blue granules in the liver after the heterodimers administration, while the liver of the rat without any heterodimers administration could not be blue stained, indicating that the Au–$Fe_3O_4$ heterodimers injected into body would accumulate in the liver and induced significant



DOI: 10.1021/acs.nanolett.9b00171
*Nano Lett.* 2019, 19, 3011–3018

enhancement both in MR and CT imaging (Figure 5c,f). It is, therefore, reasonable to conclude that the Au−$Fe_3O_4$ heterodimers developed in this study are excellent candidates for MRI/CT dual-modality imaging.

The hydrophilic nature of the heterostructures allows convenient modification of their individual components to enable more imaging modalities, therefore providing a versatile platform for integrated biomedical diagnosis and therapy. As a proof of concept, here we further demonstrate that by simply producing $Au_{shell}$-$Fe_3O_4$ heterodimers, the plasmonic resonance could be conveniently tuned to the near-infrared region (NIR, 600−900 nm) to enable their use as contrast agents for enhanced OCT and PA imaging, both of which are microscopic three-dimensional noninvasive imaging technologies. PA is an optical-absorption-based modality in which laser-generated ultrasound waves are used to obtain 3D images of soft tissues,[43] while OCT is based on optical scattering and measures the backscattered infrared light that is directed to the tissues.[44] Combining PA imaging and OCT offers the opportunity of exploiting contrast sources of each modality, providing comprehensive information on biological tissues, including the tissue anatomy, blood flow, and oxygen saturation.[45] In general, for OCT and PA imaging, the contrast nanoparticles must be less than 100 nm to prolong the blood circulation time, and their resonant absorption/scattering needs to be located in the NIR region to facilitate deep tissue penetration. As shown in Figure 6a,b, by tuning the cavity size and the thickness of the Au nanoshells, the LSPR wavelength were tuned from 636 to 864 nm. Figure 6c shows that, compared with water, Ag−$Fe_3O_4$, and $Ag_{core}$@$Au_{shell}$−$Fe_3O_4$ heterodimers, the $Au_{shell}$−$Fe_3O_4$ heterodimers displayed the greatest OCT contrast enhancement since its scattering wavelength matched that of the light source (840 nm). To test the photoacoustic signal enhancement, the agar-phantom with three types of heterodimers were scanned in sequence. As expected, $Au_{shell}$−$Fe_3O_4$ heterodimers showed the highest photoacoustic signal intensity of (2.15) than Au−$Fe_3O_4$ (0.14) and Ag@Au−$Fe_3O_4$ (0.17) heterodimers (Figure 6d), again thanks to the wavelength match. These preliminary results confirmed the potential application of the heterodimers for OCT/PA integrated imaging. Given the superparamagnetic property of $Fe_3O_4$ and high electron density of Au as mentioned above, these hybrid nanostructures could become integrated contrast agents for MRI/CT/OCT/PA multimodality imaging.

## CONCLUSIONS

In summary, we have established a general protocol for the direct synthesis of hydrophilic and biocompatible M-$Fe_3O_4$ (M = Au, Ag, and Pd) heterodimers in aqueous media. The dimension of $Fe_3O_4$ and metal parts in the heterodimers can be readily tuned in a wide range, making them ideal candidates as contrast agents for in vivo MRI and CT imaging. In addition, these heterodimers can be used as precursors to further produce more complex nanoscale heterostructures such as $AgPt_{alloy}$−$Fe_3O_4$, $Au_{core}$@$Pd_{shell}$−$Fe_3O_4$, and $Au_{shell}$−$Fe_3O_4$ heterodimers, facilitating their use as contrast agents in more imaging modalities such as OCT and PA with excellent performance. We believe this approach will make significant impacts on biomedical diagnosis and therapy by providing a general, versatile, and robust synthesis toward biocompatible multifunctional nanomaterials. By taking advantage of their magnetic/optical properties as well as the metal/oxide interfaces, these hybrid nanostructures might also find broad potential applications in optical sensing and catalysis.

## ASSOCIATED CONTENT

### Supporting Information

The Supporting Information is available free of charge on the ACS Publications website at DOI: 10.1021/acs.nanolett.9b00171.

Experimental details, TEM images, XRD patterns, UV−vis extinction spectra, digital photographs, flow cytometry analysis including Figures S1−S14 (PDF)

## AUTHOR INFORMATION


### Corresponding Authors

*E-mail: zengjb@upc.edu.cn (J.Z.).
*E-mail: hszhangd@tmmu.edu.cn (D.Z.).
*E-mail: yadong.yin@ucr.edu (Y.Y.).

### ORCID

Zifeng Yan: 0000-0002-9215-3842
Yadong Yin: 0000-0003-0218-3042


### Author Contributions

The manuscript was written through the contributions of all authors. All authors have given approval to the final version of the manuscript.

### Notes

The authors declare no competing financial interest.

## ACKNOWLEDGMENTS

This work was supported by the National Natural Science Foundation of China (Z.J., No. 21876206; G.M., No. 81501521), the Fundamental Research Funds for the Central Universities (Z.J., 18CX02037A), and the U.S. National Science Foundation (Y.Y., No. CHE-1808788).

## REFERENCES


(1) Jang, Y.; Chung, J.; Kim, S.; Jun, S. W.; Kim, B. H.; Lee, D. W.; Kim, B. M.; Hyeon, T. *Phys. Chem. Chem. Phys.* **2011**, *13*, 2512−2516.
(2) Lee, Y.; Garcia, M. A.; Frey Huls, N. A.; Sun, S. *Angew. Chem., Int. Ed.* **2010**, *49*, 1271−1274.
(3) Jin, C.; Qu, Y.; Wang, M.; Han, J.; Hu, Y.; Guo, R. *Langmuir* **2016**, *32* (18), 4595−4601.
(4) Jiang, J.; Gu, H.; Shao, H.; Devlin, E.; Papaefthymiou, G. C.; Ying, J. Y. *Adv. Mater.* **2008**, *20*, 4403−4407.
(5) Liu, J.; Liu, J.; Liu, W.; Zhang, H.; Yang, Z.; Wang, B.; Chen, F.; Chen, H. *Inorg. Chem.* **2015**, *54*, 7725−7734.
(6) Gu, H.; Yang, Z.; Gao, J.; Chang, C. K.; Xu, B. *J. Am. Chem. Soc.* **2005**, *127*, 34−35.
(7) Landgraf, L.; Christner, C.; Storck, W.; Schick, I.; Krumbein, I.; Dähring, H.; Haedicke, K.; Heinz-Herrmann, K.; Teichgräber, U.; Reichenbach, J. R.; Tremel, W.; Tenzer, S.; Hilger, I. *Biomaterials* **2015**, *68*, 77−88.
(8) Xu, C.; Wang, B.; Sun, S. *J. Am. Chem. Soc.* **2009**, *131*, 4216−4217.
(9) Parshetti, G. K.; Lin, F.-h.; Doong, R.-a. *Sens. Actuators, B* **2013**, *186*, 34−43.
(10) Yu, H.; Chen, M.; Rice, P. M.; Wang, S. X.; White, R. L.; Sun, S. *Nano Lett.* **2005**, *5*, 379−382.
(11) Xu, C.; Xie, J.; Ho, D.; Wang, C.; Kohler, N.; Walsh, E. G.; Morgan, J. R.; Chin, Y. E.; Sun, S. *Angew. Chem., Int. Ed.* **2008**, *47*, 173−176.
(12) Sun, X.; Guo, S.; Liu, Y.; Sun, S. *Nano Lett.* **2012**, *12*, 4859−4863.
(13) Ye, X.; Reifsnyder Hickey, D.; Fei, J.; Diroll, B. T.; Paik, T.; Chen, J.; Murray, C. B. *J. Am. Chem. Soc.* **2014**, *136*, 5106−5115.




DOI: 10.1021/acs.nanolett.9b00171
*Nano Lett.* 2019, 19, 3011−3018

(14) Read, C. G.; Gordon, T. R.; Hodges, J. M.; Schaak, R. E. *J. Am. Chem. Soc.* **2015**, *137*, 12514−12517.
(15) Hodges, J. M.; Morse, J. R.; Williams, M. E.; Schaak, R. E. *J. Am. Chem. Soc.* **2015**, *137*, 15493−15500.
(16) Buck, M. R.; Bondi, J. F.; Schaak, R. E. *Nat. Chem.* **2012**, *4*, 37−44.
(17) Hodges, J. M.; Schaak, R. E. *Acc. Chem. Res.* **2017**, *50*, 1433−1440.
(18) Wang, W.; Chen, X.; Efrima, S. *J. Phys. Chem. B* **1999**, *103*, 7238−7246.
(19) Lu, X.; Tuan, H.-Y.; Korgel, B. A.; Xia, Y. *Chem. - Eur. J.* **2008**, *14*, 1584−1591.
(20) Felber, M.; Alberto, R. *Nanoscale* **2015**, *7*, 6653−6660.
(21) Wang, D.; Wang, X.; Li, Z.; Chi, M.; Li, Y.; Liu, Y.; Yin, Y. *ACS Nano* **2018**, *12*, 10949−10956.
(22) Yamashita, T.; Hayes, P. *Appl. Surf. Sci.* **2008**, *254*, 2441−2449.
(23) Tan, C.; Lu, X.; Cui, X.; Jian, X.; Hu, Z.; Dong, Y.; Liu, X.; Huang, J.; Deng, L. *Chem. Eng. J.* **2019**, *363*, 318−328.
(24) Xu, W.; Wang, M.; Li, Z.; Wang, X.; Wang, Y.; Xing, M.; Yin, Y. *Nano Lett.* **2017**, *17*, 2713−2718.
(25) He, W.; Wu, X.; Liu, J.; Zhang, K.; Chu, W.; Feng, L.; Hu, X.; Zhou, W.; Xie, S. *Langmuir* **2010**, *26*, 4443−4448.
(26) Zhang, Q.; Cobley, C. M.; Zeng, J.; Wen, L.-P.; Chen, J.; Xia, Y. *J. Phys. Chem. C* **2010**, *114*, 6396−6400.
(27) Xia, Y.; Li, W.; Cobley, C. M.; Chen, J.; Xia, X.; Zhang, Q.; Yang, M.; Cho, E. C.; Brown, P. K. *Acc. Chem. Res.* **2011**, *44*, 914−924.
(28) Sun, X.; Kim, J.; Gilroy, K. D.; Liu, J.; König, T. A. F.; Qin, D. *ACS Nano* **2016**, *10*, 8019−8025.
(29) Chou, S.-W.; Shau, Y.-H.; Wu, P.-C.; Yang, Y.-S.; Shieh, D.-B.; Chen, C.-C. *J. Am. Chem. Soc.* **2010**, *132*, 13270−13278.
(30) Zhu, X.; Zhou, J.; Chen, M.; Shi, M.; Feng, W.; Li, F. *Biomaterials* **2012**, *33*, 4618−4627.
(31) Zhou, J.; Lu, Z.; Shan, G.; Wang, S.; Liao, Y. *Biomaterials* **2014**, *35*, 368−377.
(32) Zeng, Y.; Zhang, D.; Wu, M.; Liu, Y.; Zhang, X.; Li, L.; Li, Z.; Han, X.; Wei, X.; Liu, X. *ACS Appl. Mater. Interfaces* **2014**, *6*, 14266−14277.
(33) Cole, L. E.; Ross, R. D.; Tilley, J. M.; Vargo-Gogola, T.; Roeder, R. K. *Nanomedicine* **2015**, *10*, 321.
(34) Lee, N.; Choi, S. H.; Hyeon, T. *Adv. Mater.* **2013**, *25*, 2641−2660.
(35) Burtea, C.; Laurent, S.; Vander Elst, L.; Muller, R. N., Contrast agents: magnetic resonance. In *Molecular imaging I*; Springer, 2008; pp 135−165.
(36) Lee, H.; Shin, T.-H.; Cheon, J.; Weissleder, R. *Chem. Rev.* **2015**, *115*, 10690−10724.
(37) Wang, L.; Luo, J.; Fan, Q.; Suzuki, M.; Suzuki, I. S.; Engelhard, M. H.; Lin, Y.; Kim, N.; Wang, J. Q.; et al. *J. Phys. Chem. B* **2005**, *109*, 21593−21601.
(38) Zhang, S.; Qi, Y.; Yang, H.; Gong, M.; Zhang, D.; Zou, L. *J. Nanopart. Res.* **2013**, *15*, 2023.
(39) Zhou, T.; Wu, B.; Xing, D. *J. Mater. Chem.* **2012**, *22*, 470−477.
(40) Lin, F.-h.; Chen, W.; Liao, Y.-H.; Doong, R.-a.; Li, Y. *Nano Res.* **2011**, *4*, 1223−1232.
(41) Zhu, J.; Lu, Y.; Li, Y.; Jiang, J.; Cheng, L.; Liu, Z.; Guo, L.; Pan, Y.; Gu, H. *Nanoscale* **2014**, *6*, 199−202.
(42) Dou, Y.; Guo, Y.; Li, X.; Li, X.; Wang, S.; Wang, L.; Lv, G.; Zhang, X.; Wang, H.; Gong, X.; et al. *ACS Nano* **2016**, *10*, 2536−2548.
(43) Zhang, E. Z.; Povazay, B.; Laufer, J.; Alex, A.; Hofer, B.; Pedley, B.; Glittenberg, C.; Treeby, B.; Cox, B.; Beard, P.; Drexler, W. *Biomed. Opt. Express* **2011**, *2*, 2202−2215.
(44) Yang, Y.; Li, X.; Wang, T.; Kumavor, P. D.; Aguirre, A.; Shung, K. K.; Zhou, Q.; Sanders, M.; Brewer, M.; Zhu, Q. *Biomed. Opt. Express* **2011**, *2*, 2551−2561.
(45) Jiao, S.; Xie, Z.; Zhang, H. F.; Puliafito, C. A. *Opt. Lett.* **2009**, *34*, 2961−2963.



DOI: 10.1021/acs.nanolett.9b00171
*Nano Lett.* 2019, 19, 3011−3018